Optimization of Laser Metal Deposition Process for 2205 Duplex Stainless Steel

Siri Marthe Arbo[1,a], Afaf Saai[2,b*], Sture Sørli[3,c], Cato Dybdahl[1,d], Morten Onsøien[4,e] and Mette Nedreberg[5,f]

[1]Department of Materials Technology, SINTEF Manufacturing, 2830 Raufoss, Norway

[2]Department of Materials and Nanotechnology, SINTEF Industry, 7034 Trondheim

[3]Nordic Additive Manufacturing, 2830 Raufoss, Norway

[4]Department of Metal Production and Processing, SINTEF Industry, 7034 Trondheim

[5]Propulsion & Engines, Kongsberg Maritime AS, 6065 Ulsteinvik, Norway

[a]siri.marthe.arbo@sintef.no; [b]afaf.saai@sintef.no; [c]sture@nordicadditive.no;
[d]cato.dybdahl@sintef.no; [e]morten.i.onsoien@sintef.no; [f]mette.nedreberg@km.kongsberg.com

*corresponding author

Abstract. This work aims to optimize the process parameters for laser based Directed Energy Deposition (DED) manufacturing of a water jet impeller with critical requirements to material and mechanical properties. The concerned material is 2205 duplex stainless steel with balanced ferrite-austenite microstructure. The optimization approach of the processing parameters relies on the assessment of their effect on microstructure and mechanical properties versus the requirements set by the maritime industry. The work aims to achieve an as-built microstructure with the required ferrite-austenite balance and mechanical properties, without the need for post-processing heat treatment. The work particularly focuses on the influence of the deposition speed of the DED process. The results show that duplex stainless steel with a 50-50 ferrite-austenite balance can be achieved directly from the DED process. A high deposition speed produced fine-grained microstructure resulting in a high tensile strength and toughness, well above the set requirements. However, it reduced the ductility, represented by tensile elongation due to the formation of welding defects. Reducing the deposition speed by 20% eliminated the welding defects but resulted in the formation of a distinct microstructure with coarse grains, elongated in the deposited layer. This microstructure improved the tensile elongation, but strongly reduced the toughness, represented by Charpy V impact energy values. The coarse grains in the deposited layer facilitated a fast fracture propagation initiated by the placement of the Charpy V notch. However, the presented results demonstrate the great potential for manufacturing duplex stainless steels by DED, where a suitable microstructure for optimal mechanical performance can be obtained by narrowing the optimization windows on the process parameters.

Introduction

Although Additive Manufacturing (AM) promises a high potential for the maritime sector, industrial integration of AM is still hampered by technical, economical and procedural hurdles e.g., unresolved material scientific questions of the nautical sector, manufacturing challenges in the generation of large-volume components and certification of products within safety-critical applications. Among the current AM technologies, the Directed Energy Deposition (DED) processes have the greatest capability for manufacturing maritime components. This is due to the flexible process management under local inert gas atmosphere combined with very high build-up rates, even large components such as propellers or pump impellers can be manufactured. The DED processes are also ideal for multi-material applications or for combining with conventional manufacturing techniques in so-called hybrid manufacturing approaches.

In laser based DED processes, the laser beam generates a melt pool on a substrate, where the metallic powder or wire is directly deposited via a deposition head nozzle and is simultaneously melted by the laser. Then, the molten material cools down due to the feed movement of the deposition nozzle [1, 2]. The nozzle is typically managed by a 5-axis machine, where the motion paths are automatically generated based on a CAD model of the component. The direct feeding of the raw powder into the melt pool prevents the need for filling the entire build envelope. Consequently, the raw material costs of DED manufacturing scale directly with the volume of the part to be manufactured. In addition, the DED processes have great capability to generate thinner and thicker layers with precise control on the heat input by adjusting the process parameters [3].

The current work investigates the capabilities of laser based DED for manufacturing critical maritime components. The selected component is a water jet impeller, which is currently made of 2205 duplex stainless steel through conventional casting and machining. The duplex stainless steel has a dual-phase microstructure composed of a specific amount of the ferrite and austenite phases. The requirement on the microstructure is set to be 40-60% ferrite, where no intermetallic phases are allowed. Thus, the DED process must be optimized to produce the required microstructure and prevent the formation of porosity, welding defects and intermetallic phases. In addition, the DED process must produce a component that fulfills the strict requirements on mechanical properties.

The reference material and requirements are defined based on duplex stainless steel manufactured by casting, a process route that is very different compared to AM. The component produced by DED will experience a different temperature-time history which alters the microstructure, resulting in different mechanical properties [4]. In AM, both microstructure and mechanical properties are sensitive to DED process parameters, including heat input, deposition speed, layer thickness and cooling rate [4]. Thus, the optimization of such parameters is crucial to ensure the quality of the DED material and the integrity of the produced component. Experiences from manufacturing of duplex stainless steels components with AM Powder Bed Fusion or Selective laser melting has demonstrated that the high cooling rates result in predominantly a ferritic microstructure. To achieve the required microstructure with 50-50 ferrite-austenite balance, post-process heat treatment of components has been shown necessary in several studies [5-9]. When it comes to laser based DED, Iams et al. [10] and Brázda et al. [11] have demonstrated that duplex stainless steel with an austenite content between 35-45% can be directly produced by controlling the DED process parameters. This was explained by the lower cooling rates in the laser based DED, resulting in a larger formation of austenite compared to Powder Bed Fusion. Hence, the laser based DED process can be well suited for manufacturing duplex stainless-steel components, where the required microstructure can be achieved by optimizing the process parameters.

In the current work, an optimization procedure of laser based DED process parameters involving microstructure characterization and mechanical testing is established. The target is to achieve an as-built microstructure having the required ferrite-austenite balance and the required mechanical properties without post-processing heat treatments. The deposition speed was optimized to reduce the porosity and prevent welding defects that strongly affect the mechanical properties of DED parts, including toughness and ductility [2]. Standard mechanical testing methods were used to enable the evaluation of the obtained mechanical properties versus the requirements.

Experimental Procedure

Material and process. The reference material for the water jet impeller is cast 2205 duplex stainless steel of type GX2CrNiMo22-5-3, EN 1.4470. The material has a relatively high content of Cr, Mo, and Ni to improve corrosion resistance and mechanical strength. The standard AM powder for equivalent material is given by UNS S31803, ASTM 182, presented in Table 1. The chemical composition of the standard AM powder has a very small deviation compared to the chemical composition of the cast material. This small deviation is assumed to have negligible effects on material properties.

Table 1. Chemical composition of the standard AM powder for 2205 duplex stainless steel (ASTM 182)

Element	C	Cr	Mo	Mn	N	Ni	P	S	Si	Fe
[wt%]	≤ 0.03	21-23	2.5-3.5	≤ 2.0	0.8-2.0	4.5-6.5	≤ 0.03	≤ 0.02	≤ 1.0	Bal.

The DED building process was conducted using a laser metal deposition machine (Trumpf TruLaser Cell 3000) equipped with a 3000 W fiber laser. Argon gas was used as shielding gas during the build. A 90° rotation in scanning direction was applied between each successive layer.

Optimization of the DED process started with a small-scale testing step to trim the DED processing parameters. It included single bead specimens, up to 30x30 mm^2 and S-shape samples with variable thickness to replicate actual geometry, see Figure 1 (a). The goal was to identify the initial DED processing parameters, which enabled the production of a microstructure with the required ferrite-austenite balance. The outcome from this step is the initial values for laser power, spot size, powder feed rate, shield gas rate and deposition speed. Then, a building process (BP) test specimen in the form of a 75x75x130 mm^3 block was produced to extract specimens for mechanical testing, shown in Figure 1 (b). Based on the outcome from the first BP test, the deposition speed was identified as an important parameter to be investigated. Therefore, a second test specimen was produced with a reduction in deposition speed of 20%, while the other parameters were kept constant. Table 2 lists the DED process parameters used in building the two BP test specimens. The deposition speeds investigated in the current work are subjected to a non-disclose agreement and cannot be shared.

(a)   (b)

Single bead specimen   S-shape specimens

Building process test specimen
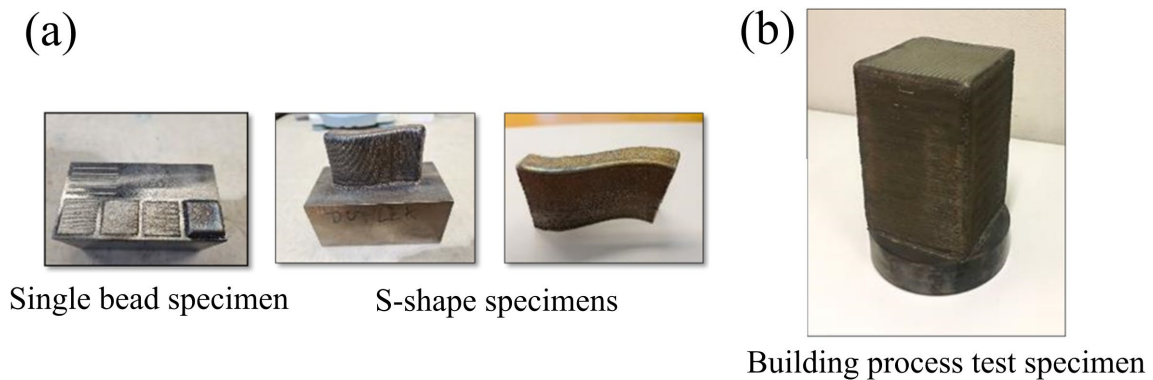
Figure 1. Steps and associated specimens involved in the optimization of process parameters From the left the right: single bead bed specimen, S-shape specimens and BP test specimen

Table 2. Process parameters used to manufacture the first and second BP specimens

Laser Power [W]	Spot size [mm]	Powder feed rate [g/min]	Shield gas rate [L/min]
2500	2	20	12

Requirements and testing methods. Specimens for mechanical testing were extracted from the two BP specimens as illustrated in Figure 2 (a). The requirements on mechanical properties of the water jet impeller include tensile strength, tensile elongation, reduction of tensile area and impact energy. To evaluate the mechanical properties versus the requirements, standard testing methods were performed. The tensile tests and Charpy V tests were performed according to EN ISO 6892-1 and EN ISO 148-1. The 3-point bending tests were performed according to ASTM E8/E8M, all according to the standard recommendation. The geometries of the testing specimens are illustrated in Figure 2 (b). To account for the effects of building and deposition directions, specimens for each test were extracted from three directions (X, Y and Z), as defined in Figure 2, where X and Y are in the deposition plan and Z represents the building direction. Three parallels were performed for each test. Note, in Figure 2 (a), specimens for cavitation tests are also included in the illustrations, but the results from these tests are not included in this work. The fracture surfaces from both tensile and Charpy V tests were studied using stereomicroscopy, optical microscopy and scanning electron microscopy (SEM). The SEM images were obtained with a working distance of 25 mm and a 20V electron beam.

The ferrite-austenite fraction was determined using a Fisher FMP30 Ferritoscope, quantifying the ferrite content based on magnetic measurements. The equipment was used on fine ground surfaces, obtaining at least 10 measurements on specimens extracted from different positions in the block. The equipment was calibrated with the appropriate standards before every use.

Specimens for microstructural analysis and hardness measurements were extracted from several locations in the produced blocks, i.e., from the surface and the center of the block, at both the bottom and top. The specimens were first ground and polished according to standard metallographic procedures, followed by an examination using optical microscopy to document defects and porosity in the structure. Next, the specimens were etched using the Beraha etch (33 ml 25% HCl, 142 ml distilled water, 1.2 grams $K_2S_2O_5$, immerse for 10 seconds), achieving a good contrast between the austenite and ferrite in the microstructure. Vickers hardness measurements were performed using a 10 kg load (HV10).
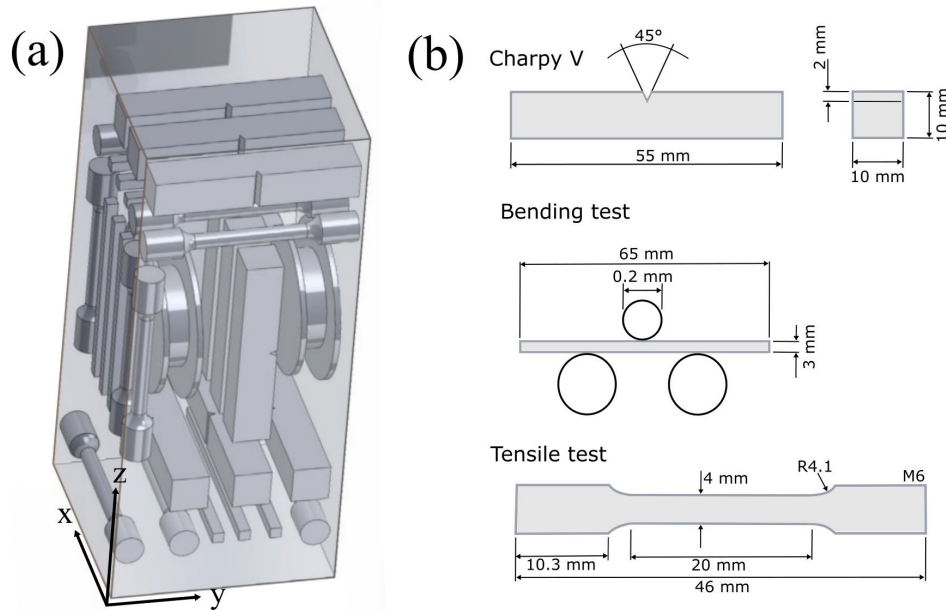
Figure 2. (a) Illustration of the position and orientation of extracted specimens for mechanical testing. **(b)** illustrations of the specimens used for tensile, Charpy V and 3-point bending tests with dimensions in mm

Results and Discussion

Material and microstructure characterization. Images of the two produced BP test specimens are shown in Figures 3 (a) and (b). It must be noted that the two BP test specimens were built on substrate materials of different sizes. For the first BP, with the highest deposition speed, the selected base material was in the same order as the produced DED specimen, see Figure 3 (a). While for the second BP, the base material was much larger than the DED specimen, see Figure 3 (b). This affects the thermal history, including the heating and cooling profiles experienced by the material depending on the distance from the base material. The effects of the base material size on microstructure and mechanical properties are discussed in the following sections.
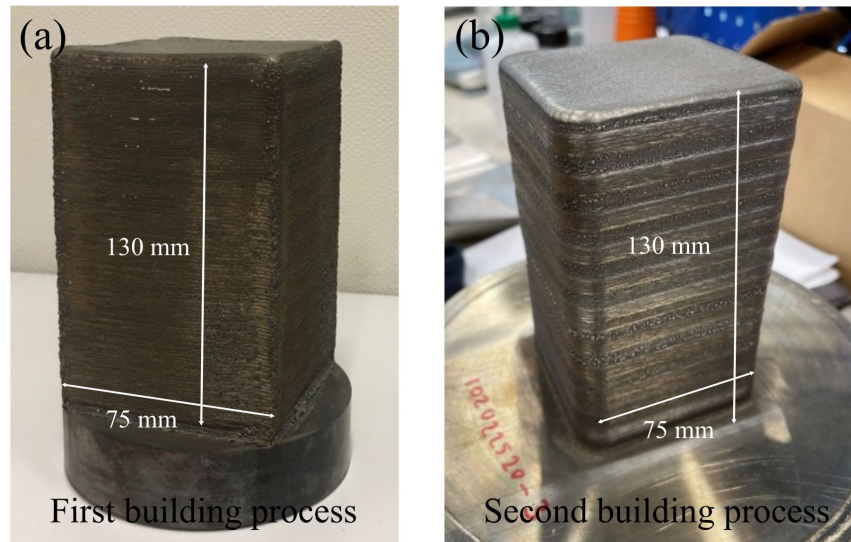
Figure 3. (a) First BP test specimen, produced on a small substrate material. **(b)** Second BP test specimen, produced on a large substrate material

First, the bulk fraction of ferrite in each specimen was evaluated. The technique has been demonstrated to give comparable results to those obtained through quantitative optical metallography point counting as described in ASTM E-562-02 [12]. The obtained measurements are presented in Table 3 for three different locations in each block.

Table 3. Ferrite content [%] measured in the two BP test specimens at three different positions

Specimen / Location	Requirement	Bottom	Middle	Top
First BP specimen	40 – 60 %	47 ± 2	50 ± 1	50 ± 1
Second BP specimen		64 ± 3	54 ± 4	51 ± 2

On average, the two BP specimens consists of a dual-phase structure with a 50-50 ferrite-austenite balance, within the set requirements (see Table 3). The first BP specimen has a homogeneous structure with a low variation in the measured ferrite fraction throughout the built. For the second BP specimen, the ferrite fraction decreases with increasing distance from the base material. The large base material (Figure 3 (b)) has resulted in a larger cooling rate in the bottom of the specimen, giving the higher ferrite content in this region. As the building height increase, more heat is accumulated in the structure, reducing the cooling rate and resulting in the formation of more austenite, as reported in the work by Iams et al. [10]. During the SEM examination of both specimens, no intermetallic phases were observed, in line with the requirements.

To evaluate the effect of deposition speed on porosity and welding defects usually observed for AM material, the polished surfaces of the two BP specimens were examined by optical microscopy. In both specimens, small spherical pores were observed, and the distributions of these pores were quite similar in the two specimens. Hence, the presence of the porosity in the two BP specimens does not seem to be influenced by the change in deposition speed. However, welding defects were observed during the examination of the first BP specimen. The defects were found to be a result of both unmelted powder, Figure 4 (b) and lack of fusion between two layers, Figure 4 (c). Similar defects were not observed in the second BP specimen, with the reduced deposition speed. Reducing the deposition speed allows the powder to melt completely by the laser, reducing the formation of such defects.
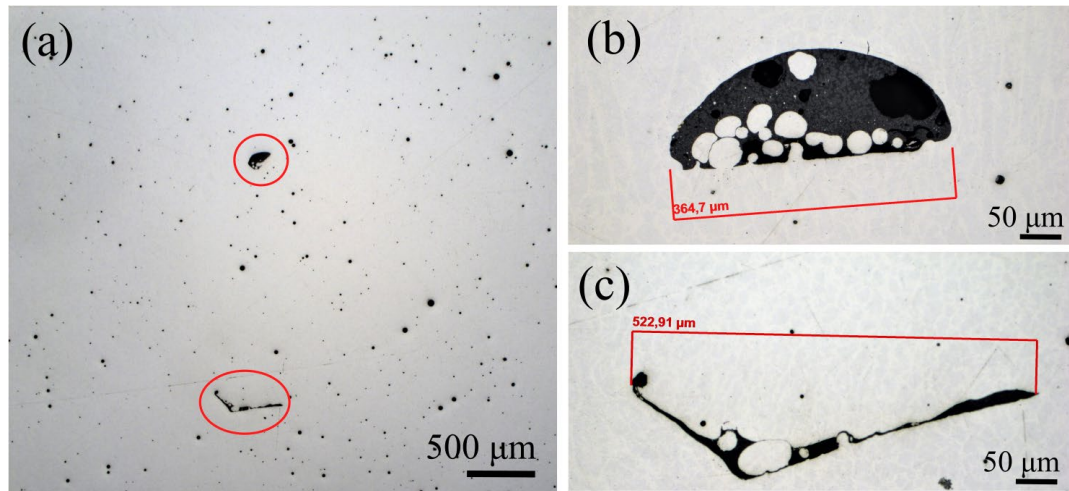
Figure 4. Optical microscopy images from the first BP specimen. **(a)** overview of the polished specimen where 2 defects can be observed. **(b)** and **(c)** high magnification images of two typically observed defects due to unmelted powder and lack of fusion

Figures 5 (a)-(d) shows optical microscopy images of the microstructure in the two BP specimens. The first BP specimen, with the high deposition speed, has a homogeneous microstructure, which does not vary with position. In the specimen, it is difficult to distinguish between the layers and the deposited tracks in the structure. However, the interface between two successive layers can be observed in some areas by the presence of elongated grains, growing parallel to the build direction (Z-direction) as shown in Figures 5 (a) and (b). In Figures 6 (a) and (b), high magnification images of the microstructure are shown for the first BP specimen. The microstructure consists mainly of very refined equiaxed grains. Austenite is found to grow mainly along the grain boundaries, while some austenite is also observed, growing into the grains with a Widmanstätten morphology, see Figure 6 (b). The microstructure observed in this first BP specimen has not previously been reported in any studies on AM of duplex stainless steel. However, it resembles the microstructure which can be observed at the fusion boundary and in the heat-affected zone of welded 2205 duplex stainless steel [13, 14].
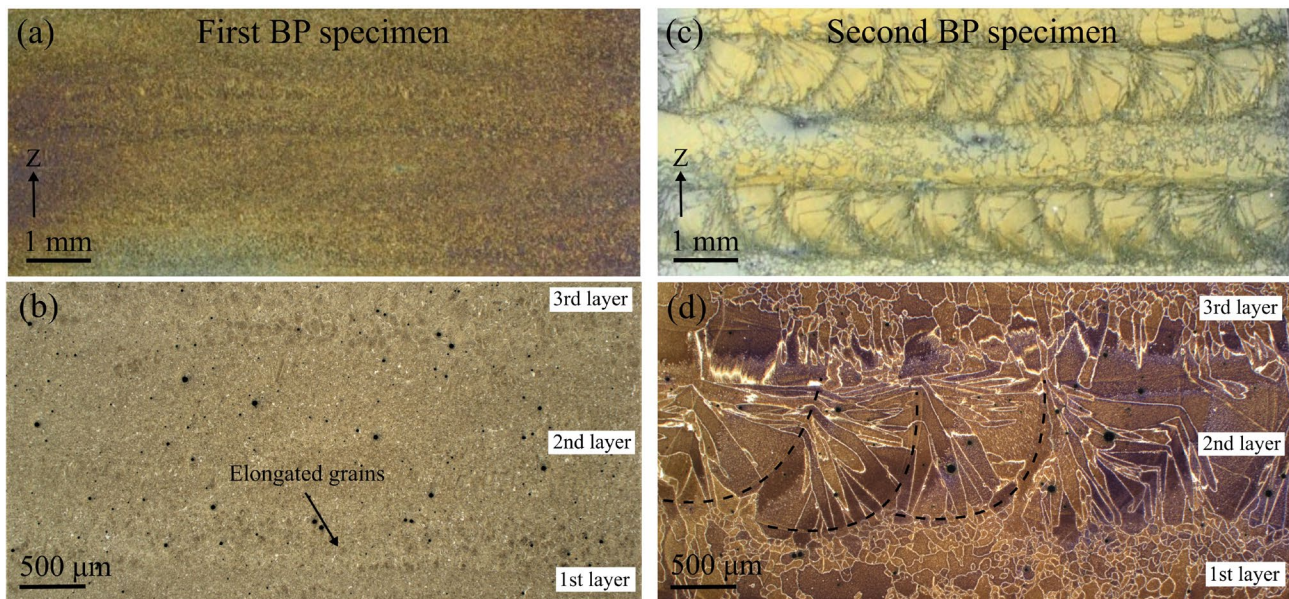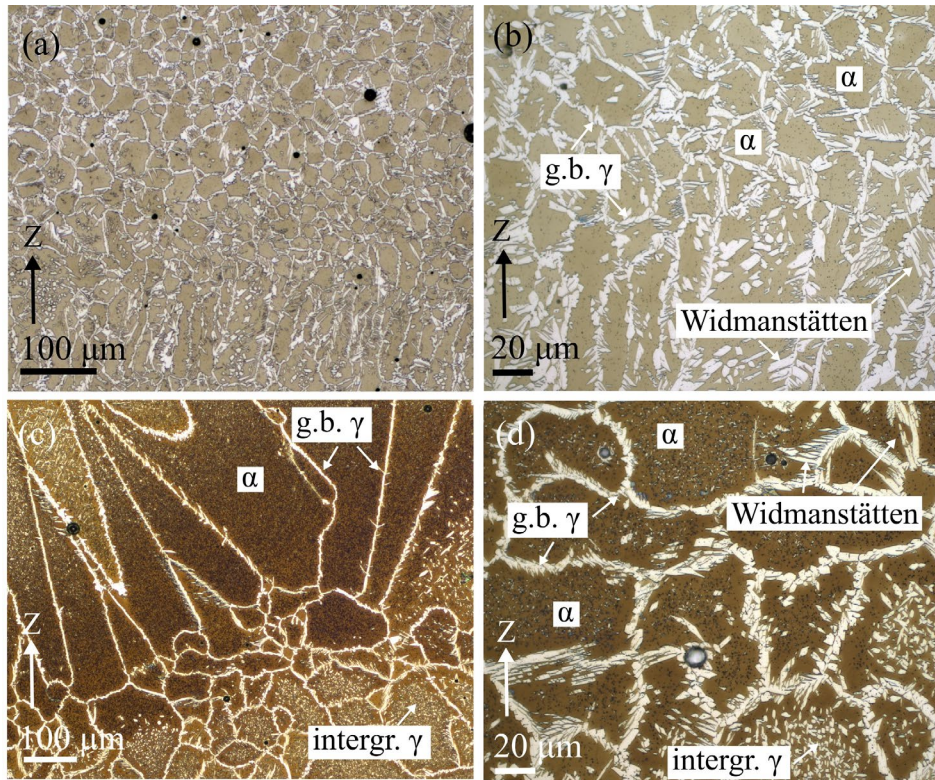

Figure 5. Representative microstructure from the center of **(a)** and **(b)** first BP specimen. **(c) and(d)** second BP specimen. **(a)** and **(c)** show low magnification optical microscopy images. **(b)** and **(c)** show high magnification optical microscopy images, where the observed layers in the structure are highlighted. Brown: ferrite (α), white: austenite (γ)

The second BP specimen, produced with a reduced speed was found to have a distinct microstructure, where each deposited layer and track could be distinguished from each other, as shown in Figures 5 (c) and (d). The black stippled lines, see Figure 5 (d), highlight the interfaces between some deposited tracks in one deposited layer. The microstructure consists of a combination of small grains along the interface between two successive layers and larger elongated grains, growing in the direction of the steepest thermal gradient towards the top of each deposited track. By analyzing the microstructure, grain boundary austenite is found together with Widmanstätten and intergranular austenite. This is shown in the high magnification images in Figures 6 (c) and (d). The distinct microstructure and austenite morphology found in the second BP specimen corresponds well with findings reported in the literature for similar AM techniques [10, 11, 15, 16].

Based on the microstructure observation, it can be argued that the reduction in deposition speed by 20% has a large influence on the microstructure. One hypothesis is that with a slow deposition speed, each deposited track solidifies prior to the deposition of the following track. Only a small part is remelted during the deposition of the next track, resulting in the distinct microstructure observed in the second BP specimen. With a higher speed, each track has not solidified separately and have instead solidified as one uniform layer. Hence, only the transition between each successive layer is observed. However, to achieve a complete understanding on how the microstructure in the first BP specimen is achieved and the mechanisms promoting this structure, more research is necessary.


Figure 6. High magnification optical microscopy images showing the microstructure and austenite morphology. **(a)** and **(b)** first BP specimen. **(c)** and **(d)** second BP specimen. Brown: ferrite (α) and white: austenite (γ)

Further investigation of the second BP specimen revealed that the microstructure changed, depending on the distance from the base material. Images taken from the top of the specimen and at the bottom, close to the base material is presented in Figures 7 (a)-(c) and (d)-(f), respectively. The overall microstructure is similar, clearly showing each deposited layer and track. However, close to the base material, most of the observed austenite is found at the grain boundaries. Only some intergranular austenite is observed, see Figures 7 (e) and (f). On the other hand, more of austenite is observed in the microstructure at the top of the BP specimen. In this region, grain boundary austenite is observed together with Widmanstätten and intergranular austenite, as highlighted in Figures 7 (b)

and (c). Thus, the austenite content increases with increasing distance from the base material, corresponding well with the presented ferrite measurements presented previously (Table 3).
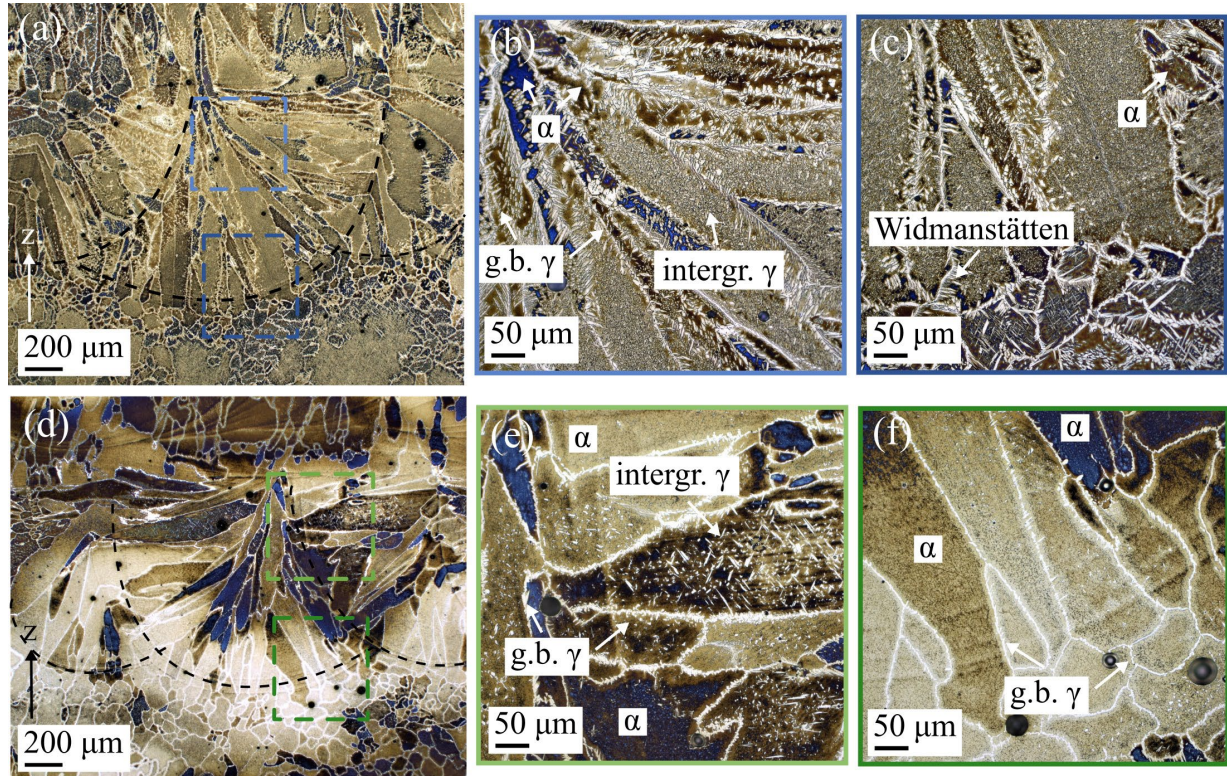

Figure 7. Microstructure in the second BP specimen. **(a)** and **(d)** shows the top and bottom of the specimen, respectively. **(b)** and **(e)** shows high magnification images of the interface between two deposited layers. **(c)** and **(f)** high magnification images of the top region of a solidified track. Brown/blue: ferrite (α) and white: austenite (γ)

Mechanical properties. The results from the mechanical tests are listed in Table 4 versus the requirements. The presented values are the average from the three parallels, ± the standard deviation for the measurements. The ferrite fraction measured in the region where the specimen for mechanical testing where extracted is also listed in Table 4. The stress-strain curves from the tensile tests are presented in Figures 8 (a) and (b) for the first and second BP specimen, respectively. The measured force as a function of displacement from the 3-point bending tests are presented in Figures 9 (a) and (b) for the first and second BP specimen, respectively.

Table 4. Results from mechanical testing of the first and second BP specimen

Properties	Req.	First BP specimen			Second BP specimen		
		X	Y	Z	X	Y	Z
Yield stress [MPa]	420	661 ± 7	676 ± 7	614 ± 9	718 ± 14	548 ± 9	611 ± 9
Tensile stress [MPa]	600	893 ± 2	890 ± 6	828 ± 7	857 ± 11	802 ± 3	866 ± 4
Elongation at fracture [%]	20	20 ± 1	18 ± 2	14 ± 1	17 ± 2	28 ± 1	24 ± 1
Charpy V [J]	30	79 ± 4	50 ± 2	86 ± 6	7 ± 0	43 ± 1	19 ± 1
Bending angle [°]	-	115 ± 1	115 ± 0	116 ± 0	120 ± 6	143 ± 0	130 ± 1
Ferrite fraction [%]	40-60	47 ± 2	50 ± 1	50 ± 1	64 ± 3	51 ± 2	54 ± 4
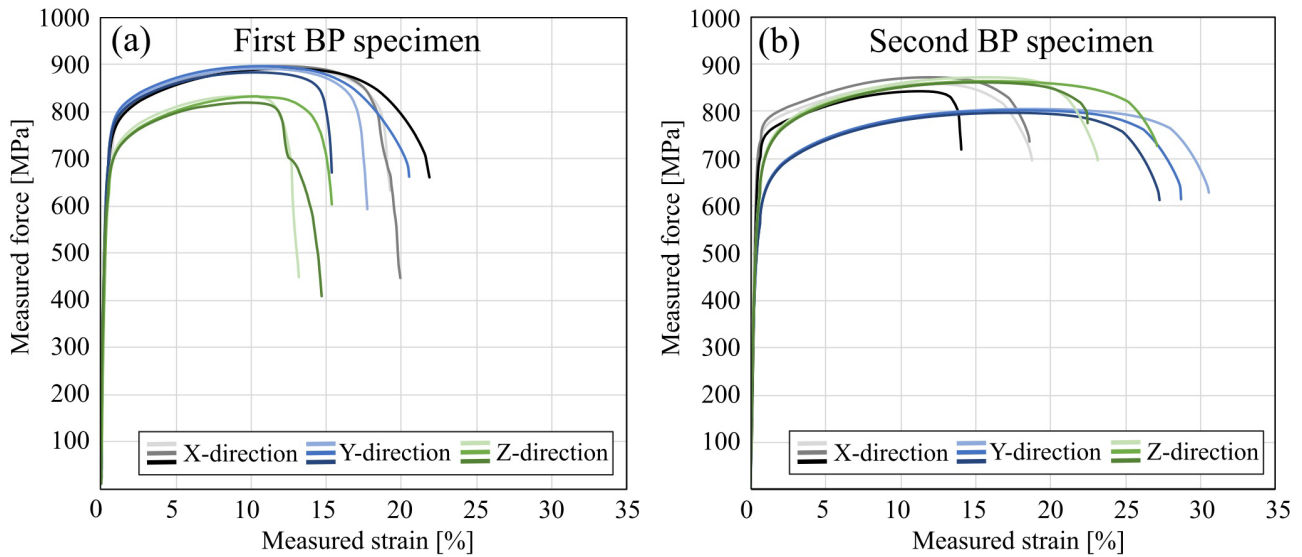
Figure 8. Measured stress-strain curves from performed tensile tests for **(a)** the first BP specimen with high deposition speed and **(b)** the second BP specimen with a 20% lower deposition speed
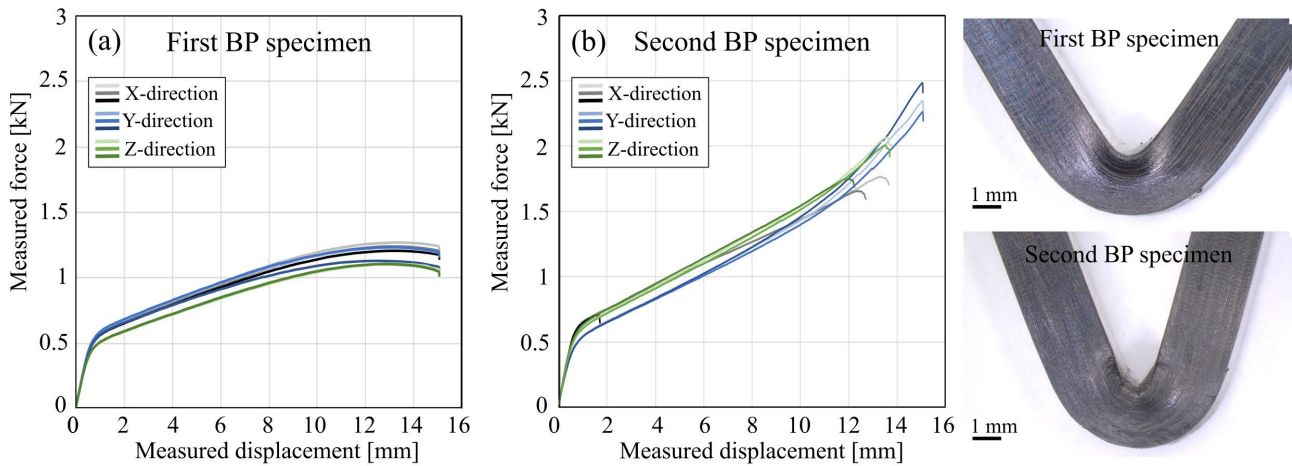

Figure 9. Measured force-displacement curves from performed 3-point bending tests for **(a)** the first BP specimen with a high deposition speed and for **(b)** the second BP specimen, with a 20% lower speed. **(c)** and **(d)** shows a representative 3-point bending test specimen for the first and second BP, respectively

For the first BP specimen with the highest deposition speed, the tensile tests demonstrate high yield and tensile strengths in all directions, higher than the requirements set for the impeller. This might be explained by the refined microstructure obtained at higher deposition speed as demonstrated in Figure 5 and Figure 6. The strength of the specimens extracted from the build-direction (Z-direction) is lower than the strength of the specimens extracted from the building plane (X- and Y-directions), which show similar responses. Similar anisotropy was also observed on the tensile elongation, where the lowest values were associated with the specimens extracted from the building direction. The tensile elongation for this first BP specimen did not meet the requirement of 20%. The impact energy measured by Charpy V tests is also high in all directions, higher than the required impact energy for the impeller reference material. The high toughness is due to the fine-grained microstructure resulting from the high deposition speed. The lowest impact energy was associated with Charpy V specimens oriented in Y-direction, where the notch is oriented parallel to the Z-direction. The results from the bending tests correlate with the results from the tensile tests, where the bending specimens have a moderate bending angle. The fracture surfaces from the tensile tests were further analyzed to investigate the cause for the low elongation and is presented in the next section.

The second BP specimen with a 20% reduced deposition speed had an uneven distribution of ferrite, which increased with increasing distance from the base material on which the specimen was built. The bottom part of the specimen has the higher ferrite content (approximately 64%), which decreases to 50% of ferrite in the upper side of the specimens. As illustrated in Figure 2 (c), the specimens for mechanical testing oriented in the X-direction were extracted from the bottom region, while the specimens for mechanical testing oriented in Y-direction were extracted from the upper region. From the results listed in Table 4, it is found that the higher ferrite content has resulted in a higher strength, lower ductility, and poor impact toughness for X-direction (bottom) specimens compared to Y-direction (upper) specimens. The Y-direction and Z-direction specimens in the second BP specimen have a similar ferrite-austenite balance as the first BP specimen of 50-50, see Table 4. From the measured tensile elongation, it can clearly be observed that the reduction of deposition speed improves the ductility. The result from bending tests corresponds well with the results from the tensile tests, showing a clear improvement of the material ductility.

Compared to the requirements on impeller reference material, the measured tensile properties fulfill the given requirements on strength and elongation. However, when it comes to impact properties, the impact energies measured by the Charpy V tests have large deviations and are below the requirement in both the X- and Z-direction. This might be explained by the combined effects of the non-homogeneous distribution of ferrite, coarse grain formation and distinct microstructure resulting from the reduction of deposition speed, presented in the previous section. Further investigation of the surface fracture was performed to study the effects of such microstructure on fracture propagation.

Fracture surfaces. The fracture surfaces of selected tensile and Charpy specimens were examined by SEM to investigate the fracture cause. Figures 10 (a)-(d) show SEM images obtained from one of the tensile test specimens from the first BP specimen, where the observed defects are highlighted. Areas with unmelted powder and flat areas without dimples, indicating a lack of fusion is observed, see Figures 10 (b) and (d). The rest of the fracture surface consisted of a fine dimpled structure, indicating a ductile material. Thus, the analyses confirmed that the presence of welding defects is the main reason for the low elongation found in the first BP specimen.
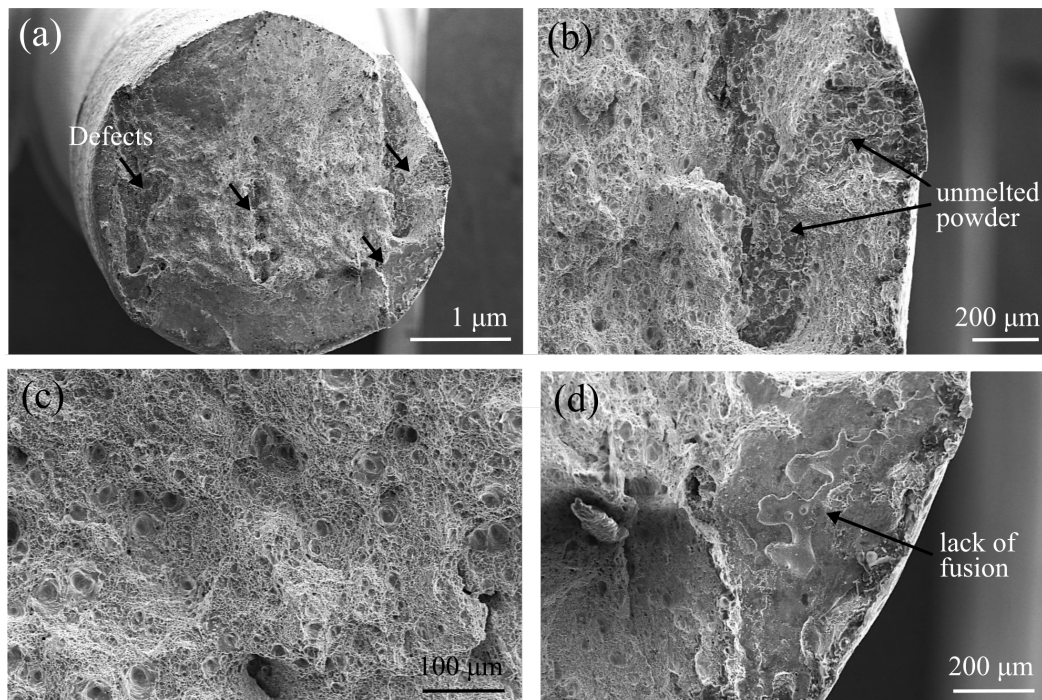
Figure 10. SEM images of the fracture surface for a tensile test specimen, oriented parallel to the build direction (Z-direction) from the first BP specimen. **(a)** overview of entire fracture surface showing several defects. **(b)** Area with unmelted powder. (c) Area of fracture surface containing small dimples. **(d)** Flat area on surface indicating lack of fusion between two successive layers

Figures 11 (a) and (b) show stereomicroscope images of the Charpy V specimens extracted from the second BP specimen, in the Z-direction. The notch is placed parallel with the X-direction. The specimen has been polished perpendicular to the fracture surface, allowing the fracture propagation path in the microstructure to be examined. Figures 11 (a) and (b) show how the fracture has propagated directly through one deposited layer, where the notch originally was placed. In this region, the microstructure consists of large ferrite grains with various degrees of intergranular austenite, allowing for a fast fracture propagation, see Figures 11 (c) and (d). In future work, it is necessary to focus on eliminating this microstructure, where each track and layer clearly can be separated, achieving a microstructure closer to the first BP specimen, without the defects to improve the impact properties.
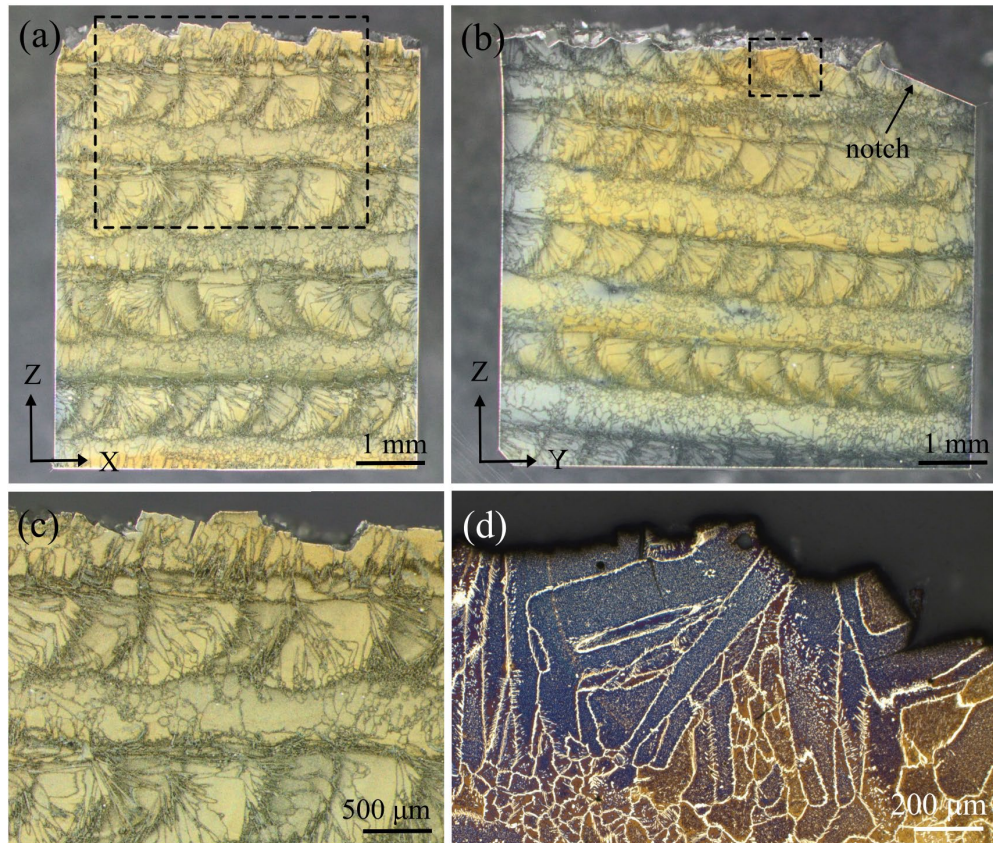
Figure 11. Stereomicroscopy images showing two polished cross-sections of a Charpy V specimen from the second BP extracted from the build direction (Z-direction). **(a)** and **(b)** show the microstructure of the fractured specimen in the Z-X and Z-Y planes, respectively. The notch is placed perpendicular to the building direction and parallel to the X-direction. **(c)** and **(d)** show optical microscopy images of the highlighted areas in (a) and (b). Fracture has propagated through one deposited layer

As stated by Bajaj et al. [4], the tensile strength of steel components produced by AM typically matches or exceeds conventionally produced components. This is true for both the first and second BP specimens produced in this study. On average, the mechanical properties achieved in this study are superior to the requirements based on casted material. However, as shown, the properties are sensitive to welding defects, achieved microstructure and the ferrite-austenite balance, which all must be optimized through the correct selection of process parameters.

Conclusion

The effect of deposition speed in laser based DED process on the microstructure and mechanical properties of 2205 duplex stainless steel were investigated by the mean of mechanical testing and microstructure characterization. Two building processes with a 20% difference in the deposition speed were evaluated. The relationship between deposition speed, material microstructure and mechanical properties were established. The results from mechanical testing and microstructure characterizations can be summarized in the following highlights:

- The microstructure is strongly affected by deposition speed. A high deposition speed creates a uniform refined microstructure with no clear interfaces indicating the deposited tracks in the structure. Reducing the deposition speed results in a distinct and coarser microstructure where each deposited track and layer could be observed. However, both investigated deposition speeds provided a 50-50 ferrite-austenite balance in the structure.
- Variations in the ferrite-austenite balance were found when the base material was much larger than the produced components. An increased ferrite content was found close to the base material, due to higher cooling rates at the beginning of the building process, reducing the ductility and toughness in this region compared to the areas with a 50-50 ferrite-austenite balance.
- The higher deposition speed resulted in the formation of welding defects, reducing the ductility of the material, represented by tensile elongation and bending angle. The presence of welding defects was eliminated by reducing the deposition speed by 20%.
- The distinct microstructure formed at the lowest investigated deposition speed strongly affected the mechanical properties. The strength of the material, represented by the yielding and ultimate tensile stresses were slightly reduced. The toughness, represented by Charpy V impact energy was also reduced, due to the coarse microstructure which facilitated a fast fracture propagation, initiated from the specimen notch.

The evaluation of material properties versus the requirements demonstrates great potential of DED manufacturing for critical duplex stainless steel components. Optimized control of DED processing parameters enables the production of material with a suitable microstructure. However, a suitable base material selection must be considered to ensure the required fraction of the phases throughout the entire component. In this context, the numerical simulations which account for the effect of geometry on thermal history are appreciated. The obtained results demonstrate the possibility for DED manufacturing of duplex stainless-steel material with the required properties by controlling the process parameters.

References

[1] E.M. Birger, G.V. Moskvitin, A.N. Polyakov and V.E. Arkhipov, Industrial laser cladding: current state and future, Weld. Int. 25 (2011) 234-243.

[2] B. Graf, S. Ammer, A. Gumenyuk and M. Rethmeier, Design of Experiments for Laser Metal Deposition in Maintenance, Repair and Overhaul Applications, Procedia CIRP 11 (2013) 245-248.

[3] D. Boisselier, S. Sankaré and T. Engel, Improvement of the Laser Direct Metal Deposition Process in 5-axis Configuration, Phys. Procedia 56 (2014) 239-249.

[4] P. Bajaj, A. Hariharan, A. Kini, P. Kürnsteiner, D. Raabe and E.A. Jägle, Steels in additive manufacturing: A review of their microstructure and properties, Mater. Sci. Eng. A 772 (2020).

[5] N. Haghdadi, M. Laleh, M. Moyle and S. Primig, Additive manufacturing of steels: a review of achievements and challenges, J. Mater. Sci. 56 (2020) 64-107.

[6]   S. Papula, M. Song, A. Pateras, X.B. Chen, M. Brandt, M.Easton, Y. Yagodzinskyy, I. Virkkunen and H. Hanninen, Selective Laser Melting of Duplex Stainless Steel 2205: Effect of Post-Processing Heat Treatment on Microstructure, Mechanical Properties, and Corrosion Resistance, Mater. 12 (2019).

[7]   G.N. Nigon, O. Burkan Isgor and S. Pasebani, The effect of annealing on the selective laser melting of 2205 duplex stainless steel: Microstructure, grain orientation, and manufacturing challenges, Opt. Laser Technol. 134 (2021).

[8]   F. Hengsbach, P. Koppa, K. Duschik, M.J. Holzweissig, M. Burns, J. Nellesen, W. Tillmann, T. Tröster, K.P. Hoyer and M. Schaper, Duplex stainless steel fabricated by selective laser melting - Microstructural and mechanical properties, Mater. Des. 133 (2017) 136-142.

[9]   K. Davidson and S. Singamneni, Selective Laser Melting of Duplex Stainless Steel Powders: An Investigation, Mater. Manuf. Process. 31 (2016) 1543-1555.

[10]   A.D. Iams, J.S. Keist and T.A. Palmer, Formation of Austenite in Additively Manufactured and Post-Processed Duplex Stainless Steel Alloys, Metall. Mater. Trans. A 51 (2019) 982-999.

[11]   M. Brázda, P. Salvetr, J. Dlouhý and J. Vavřík, Influence of laser power in direct laser deposition on the proportion of ferrite and austenite in duplex steel SAF2507, METAL 2020 Conference Proeedings (2020) 539-544.

[12]   A.F. Junior, J. Otubo and R. Magnabosco, Ferrite Quantification Methodologies for Duplex Stainless Steel, J. Aerosp. Technol. Manag. 8 (2016).

[13]   A. Ureña, E. Otero, M.V. Utrilla and C.J. Múnez, Weldability of a 2205 duplex stainless steel using plasma arc welding. J. Mater. Process. Technol. 182 (2007) 624-631.

[14]   S. Topolska and J. Łabanowski, Environmental Degradation of Dissimilar Austenitic 316L and Duplex 2205 Stainless Steels Welded Joints, Arch. Metall. Mater. 62 (2017).

[15]   V.A. Hosseini, M. Högström, K. Hurtig, M.A. Valiente Bermejo, L.E. Stridh and L. Karlsson, Wire-arc additive manufacturing of a duplex stainless steel: thermal cycle analysis and microstructure characterization, Weld World 63 (2019) 975-987.

[16]   M.A. Valiente Bermejo, K. Thalavai Pandian, B. Axelsson, E. Harati, A. Kisielewicz and L. Karlsson, Microstructure of laser metal deposited duplex stainless steel: Influence of shielding gas and heat treatment, Weld World 65 (2020) 525-541.